

Interferometric visibility of single-lens models: the thin-arcs approximation

Arnaud Cassan^{*}

Institut d'Astrophysique de Paris, Sorbonne Université, CNRS, UMR 7095, 98 bis bd Arago, F-75014 Paris, France

Received / Accepted

ABSTRACT

Long-baseline interferometry of microlensing events can resolve the individual images of the source produced by the lens, which combined with the modeling of the microlensing light curve, lead to the exact lens mass and distance. Interferometric observations thus offer a unique opportunity to constrain the mass of exoplanets detected by microlensing, and to precisely measure the mass of distant isolated objects such as stars, brown dwarfs and stellar remnants like white dwarfs, neutron stars or stellar black holes. Having accurate models and reliable numerical methods is of particular importance, as the number of targets is expected to increase significantly in the near future. In this work, we discuss the different approaches to calculating the fringe complex visibility for the important case of a single lens. We propose a robust integration scheme to calculate the exact visibility, and introduce a novel approximation, that we call ‘thin-arcs approximation’, which applies over a wide range of lens-source separations. We find that this approximation runs $\times 6$ to $\times 10$ times faster than the exact calculation, depending of the characteristics of the event and the required accuracy. This approximation provides accurate results for microlensing events of medium to higher magnification observed around the peak, *i.e.* a large fraction of potential observational targets.

Key words. Gravitational lensing: micro, Techniques: interferometric, Methods: numerical

1. Introduction

Measuring the mass of isolated objects in our Milky Way is a major challenge in astrophysics, whether it be the mass of stars, brown dwarfs or stellar remnants such as white dwarfs, neutron stars or stellar black holes. In fact, few observational techniques allow such measurements to be made with high precision and/or independently of assumptions about the structure of the targeted objects. Gravitational microlensing (Paczynski 1986), based on the deflection of light rays by a lensing body transiting the line of sight of a distant star, provides a solution of choice for measuring the mass of such isolated lenses. The technique allows to probe objects intrinsically luminous or not, up to Galactic scales and independently of the light emitted by the lens itself.

Microlensing affects the shape and the number of images of the source star, which results in a global enhancement of the total flux received by the observer. As the individual images produced by the microlens cannot be separated by classical telescopes, what is usually measured is the increase (or magnification) of the flux of the source star as a function of time. Nevertheless, when for bright enough microlensing events, the lensed images can in principle be resolved with long-baseline interferometers (Delplancke et al. 2001; Dalal & Lane 2003; Rattenbury & Mao 2006; Cassan & Ranc 2016), since their typical separation is of the order of a milliarcsecond, *i.e.* within the reach of interferometers with baselines of a few tens or a hundred metres. As a matter of fact, a first series of successful interferometric observations were recently made with the Very Large Telescope Interferometer (ESO/VLTI), on microlensing events TCP J05074264+2447555 ‘Kojima-1’ (Dong et al. 2019) and Gaia19bld (Cassan et al. 2021).

To measure the mass of the lens, two quantities must be derived from the observations: π_E , the microlensing parallax; and θ_E , the angular Einstein ring radius, that is, the angular radius of the ring-like image of the source would it be perfectly aligned with the lens. The mass follows from $M = \theta_E / \kappa \pi_E$, where $\kappa = 8.144 \text{ mas}/M_\odot$ (Gould 2000). Ground-based observations can access π_E for long-lasting microlensing events, for which the transverse motion of the Earth is significant enough to allow a good parallax measurement, while for shorter microlensing events, space-based parallax is in general required to provide a different vantage point from Earth. Classically, θ_E may be estimated from the photometric light curve if the spatial extension of source reveals itself by producing noticeable deviations in the light curve, and if the source star is well characterised; or, in the case of bright microlenses, high-resolution, adaptive-optics imaging may also access θ_E typically 5-10 years after the microlensing event is over, when the background star and the microlens can be resolved individually. As for long-baseline interferometry, it provides a direct measurement of θ_E by resolving the split images of the source star and measure their angular separations. When times-series observations are performed, an additional constraint on π_E can be further obtained (Cassan et al. 2021).

The modelling of interferometric data requires both robust and efficient numerical methods to compute the microlensing models, with a good control on numerical errors, in order to calculate the wide range of models typically required by Markov Chain Monte Carlo (MCMC) algorithms. In this work, we discuss in detail the case of single-lens models. In Section 2, we propose a new and more efficient approach for the exact calculation of the complex interferometric visibility than what exists in the literature; we also establish a new approximation, the ‘thin-

^{*} arnaud.cassan@iap.fr

arcs approximation', which runs $\times 6$ to $\times 10$ times faster than the exact calculation and should apply to a large fraction of potential observational targets. In Section 3, we illustrate and discuss the domain of validity of the thin-arcs approximation by comparing it to the exact calculation, and also to the point-source approximation. We further discuss possible shortcomings of ill-defined parameterisations, and advocate for suitable sets of parameters depending on the characteristics of the observed microlensing event. We conclude in Section 4.

2. Visibility of reference single-lens models

2.1. Key concepts and equations

The lens equation relates the angular position of the background source star to that of its multiple images. If we set up a cartesian frame of reference (O, x, y) with axes fixed in the plane of the sky (e.g. North, East) and if we choose the lens to stand at the center of the coordinate system, the complex lens equation for an isolated massive body reads

$$\zeta = z - \frac{1}{\bar{z}}, \quad (1)$$

where ζ is the affix of the (point-like) center of the source, z the affix of one of the individual point-like image and \bar{z} the complex conjugate of z . For the lens equation to be correct, the quantities ζ and z are further normalised by θ_E , the Einstein angular ring radius (Einstein 1936), which is a function of the lens mass M , the observer-lens distance D_L and the observer-source distance D_S through

$$\theta_E \equiv \sqrt{\frac{4GM}{c^2} \left(\frac{D_S - D_L}{D_S D_L} \right)}, \quad (2)$$

with c is the speed of light and G the gravitational constant. The typical separation of the images is of order of θ_E ; when the source, lens and observer are perfectly aligned, the image is seen as a perfect ring-shaped image, called 'Einstein ring'. For a given position $\zeta = u_1 e^{i\theta}$ of the source center \mathcal{S} (Figure 1), the single lens equation Eq. (1) is easily solved by writing $z = r e^{i\theta}$, with r solution of $r^2 - u_1 r - 1 = 0$. This yields two solutions for the images, $z^{(\pm)} = r^{(\pm)} e^{i\theta}$, where

$$r^{(\pm)} = \frac{u_1 \pm \sqrt{u_1^2 + 4}}{2}. \quad (3)$$

If we assume $u_1 > 0$, the image with $r^{(+)} > 0$ is the major image ($\mathcal{I}^{(+)}$ in Figure 1) and that with $r^{(-)} < 0$ is the minor image ($\mathcal{I}^{(-)}$ in the figure). As ζ , $z^{(+)}$ and $z^{(-)}$ have same argument, \mathcal{S} , $\mathcal{I}^{(+)}$, $\mathcal{I}^{(-)}$ are aligned together with the lens, as shown in Figure 1. If the lens is perfectly aligned with the lens, *i.e.* $\zeta = 0$, then Eq. (1) yields $|\zeta| = 1$ and the image is an Einstein ring, of physical angular radius θ_E . To avoid any confusion in the units in the angular quantities we are going to discuss, in the following we assign a subscript 'E' to all angular coordinates expressed in θ_E units. Hence we will write $\zeta \equiv \xi_E + i\eta_E$ and $z \equiv x_E + iy_E$, with

$$(x_E, y_E) \equiv (x, y) / \theta_E, \quad (4)$$

where (x, y) are expressed in radians and (x_E, y_E) in θ_E units.

The complex (fringe) visibility measured by the interferometer is the Fourier transform of the spatial distribution of light

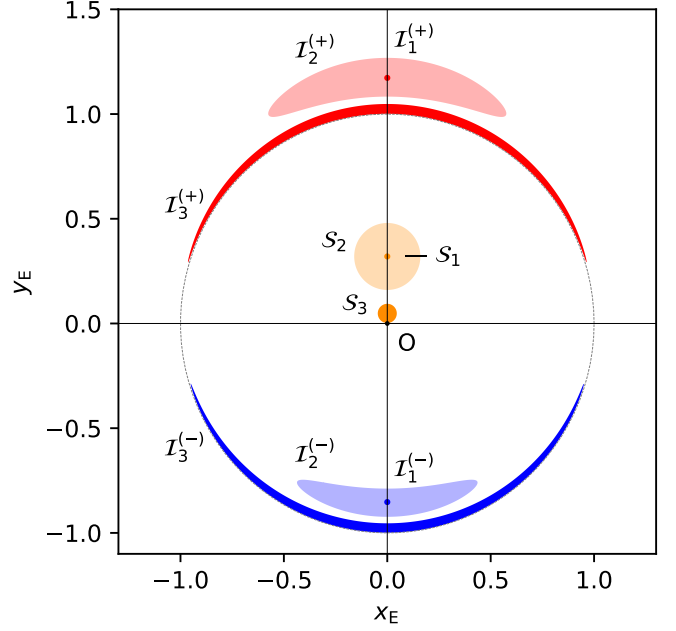


Fig. 1. Schematics of the three reference single-lens models detailed in the text. In all cases, the source center lies onto the y_E -axis, and the source surface is uniformly bright. Both axes are in θ_E units. The microlens is the black dot at the center of the frame, and the Einstein ring is marked by the dotted-line circle of radius unity. In the point-source approximation, the source star \mathcal{S}_1 (in orange) is point-like and has two point-like images: the major image $\mathcal{I}_1^{(+)}$ (in red) is located outside of the Einstein ring, while the minor image $\mathcal{I}_1^{(-)}$ (in blue) is lying inside of it. In general, a source as \mathcal{S}_2 has a spatial extension, and its major and minor images $\mathcal{I}_2^{(+)}$ and $\mathcal{I}_2^{(-)}$ are elongated along the Einstein ring. When both the source radius and the lens-source separation are small compared to unity, as for source \mathcal{S}_3 , the two images take the form of two thin arcs, $\mathcal{I}_3^{(+)}$ and $\mathcal{I}_3^{(-)}$. When the microlens lies inside the source, the two images merge into a single ring-like image (not shown here).

$I(x_E, y_E)$ in the plane of the sky (more precisely here: the surface brightness of the images), or

$$\mathcal{F}[I](u_E, v_E) \equiv \iint_{\mathbb{R}^2} I(x_E, y_E) e^{-i2\pi(u_E x_E + v_E y_E)} dx_E dy_E, \quad (5)$$

where (u_E, v_E) are the conjugate coordinates of (x_E, y_E) . The latter are thus expressed as

$$(u_E, v_E) \equiv (u, v) \times \theta_E, \quad (6)$$

where (u, v) are the usual spatial frequencies, related to the projected baselines B_u and B_v (respectively in the (Ox) and (Oy) directions) by $u = B_u/\lambda$ and $v = B_v/\lambda$, with λ the wavelength of observations; but while (u, v) are expressed in radians, (u_E, v_E) are in θ_E^{-1} units (Cassan & Ranc 2016). Hereafter, we also call visibility the quantity

$$V_E(u_E, v_E) \equiv \frac{\mathcal{F}[I](u_E, v_E)}{\mathcal{F}[I](0, 0)}, \quad (7)$$

which is a normalised version of Eq. (5), as the term in the denominator is the total flux. The squared visibility is the squared modulus of the visibility, $|V_E|^2$, and its phase is $\phi = \arg V_E$.

Let us now consider a circular, uniformly bright source of constant surface brightness $I(x_E, y_E) = I_S$, lensed by an isolated

massive body (limb-darkened sources will be treated in Section 2.5). As I_S cancels out in the expression of V_E in Eq. (7), it is convenient to use the quantity $\Phi \equiv \mathcal{F}[I]/I_S$ (that we will also call visibility for simplicity); for the lensed images, we then have

$$\Phi_{\mu l}(u_E, v_E) = \iint_I e^{-i2\pi(u_E x_E + v_E y_E)} dx_E dy_E, \quad (8)$$

where the subscript ‘ μl ’ stands for ‘microlensed’. The integration is performed within the boundaries I of the (multiple) lensed images. These images are elongated around the Einstein ring, as shown in Figure 1 for the S_2 and S_3 sources.

Beside the lensed images of the source, bright stars in the observing line-of-sight, although not magnified by the lens, may also be considered as contributing ‘blend’ stars of total visibility Φ_B . In particular, if the lens itself is bright enough, it may indeed contribute to a blend term Φ_L . Other stars than the lens are unlikely to be involved, even in crowded fields in the Galactic bulge region, because most stars in the immediate vicinity of the lens are faint. We define the blending factor of individual blend star k as the ratio $g_k \equiv F_{B_k}/F_S$, where F_{B_k} is the flux of blend star k and $F_S = I_S S$ the flux of the source when it is not lensed, with $S = \pi\rho^2$ and ρ the radius of the source in θ_E units. We justify that I_S is used to calculate the flux of both the source and its lensed images, as gravitational lensing has the important property to preserve surface brightness when forming the lensed images. For a given blend star k of surface S_k (in θ_E^2 units), the star’s (constant) surface brightness reads $I_{B_k} \equiv F_{B_k}/S_k = g_k I_S/S_k$. As in general these stars are not resolved by the interferometer (including the lens: a typical solar-mass lens at 4 kpc has an angular diameter of about $2 \mu\text{as}$), S_k can be considered infinitely small and we may write $I_{B_k} = g_k I_S \delta(x_E - x_{E_k}) \delta(y_E - y_{E_k})$, with δ the Dirac distribution and (x_{E_k}, y_{E_k}) the coordinates of star k . Considering all blend stars, the surface brightness reads

$$I_B(x_E, y_E) = \sum_k I_{B_k} = I_S \pi\rho^2 \sum_k g_k \delta(x_E - x_{E_k}) \delta(y_E - y_{E_k}), \quad (9)$$

so that the blend visibility is given by

$$\Phi_B(u_E, v_E) = \pi\rho^2 \sum_k g_k e^{-i2\pi(u_E x_{E_k} + v_E y_{E_k})}. \quad (10)$$

In particular, a bright lens (in the center of the frame) would contribute to $\Phi_L = g_L \pi\rho^2$, with $g_L = F_L/F_S$ the blend to source flux ratio. As for the overall visibility, it is expressed as

$$V_E(u_E, v_E) = \frac{\Phi_{\mu l} + \Phi_B}{\Phi_{\mu l_0} + \Phi_{B_0}}, \quad (11)$$

where $\Phi_{\mu l_0} \equiv \Phi_{\mu l}(0, 0)$ and $\Phi_{B_0} \equiv \Phi_B(0, 0)$. When three or more baselines are involved, the bispectrum $B_{E,1,2,3}$ and closure phase $\phi_{E,T3}$ of each triangle of baselines are given by

$$B_{E,1,2,3} = V_E(u_{E,1}, v_{E,1}) \times V_E(u_{E,2}, v_{E,2}) \times V_E(u_{E,3}, v_{E,3}), \quad (12)$$

$$\phi_{E,T3} = \arg(B_{E,1,2,3}), \quad (13)$$

where $(u_{E,3}, v_{E,3}) = -(u_{E,1}, v_{E,1}) - (u_{E,2}, v_{E,2})$ (or an equivalent formula considering that $V_E(-u_E, -v_E) = \overline{V_E(u_E, v_E)}$).

For an interferometer observing in the H band ($\lambda \approx 1.65 \mu\text{m}$) with projected baseline $B = 100$ m along the x -axis, and typical values of θ_E of 0.5, 1, 1.5 and 2 mas, the interferometer will probe u_E -values of 0.15, 0.30, 0.45 and 0.60 (in θ_E^{-1} units). As the angular separation of the major and minor images is $\sim 2 \times \theta_E$ (cf. Figure 1), we expect the visibility to be modulated with a

period of ~ 0.5 along u_E , with a first minimum at $u_E \sim 0.25$ (in θ_E^{-1} units). It means that provided the microlensing event is bright enough to be observed, the lensed images can be resolved in most cases, and the value of θ_E measured.

In the following sections, we derive suitable formulae to compute efficiently Eq. (8) for three reference single-lens models: the point-source approximation, the exact formula and a novel ‘thin-arcs approximation’, for uniform and limb-darkened sources.

2.2. The point-source approximation

The visibility for a single lens in the point-source approximation was first studied by Delplancke et al. (2001). Here, we start with a more general situation where a lens made of multiple bodies produces more than two point-like images of the source. If F_S is the non-magnified flux of the source, similar to what was done in Section 2.1 we write the surface brightness of the source as

$$I(\xi_E, \eta_E) = F_S \delta(\xi_E - \xi_{E_S}) \delta(\eta_E - \eta_{E_S}), \quad (14)$$

where (ξ_{E_S}, η_{E_S}) are the coordinates of the source in θ_E (angular) units. The lens equation $(x_E, y_E) \rightarrow (\xi_E, \eta_E)$ describes how the coordinates of the source (ξ_{E_S}, η_{E_S}) are transformed into multiple images i of coordinates (x_{E_i}, y_{E_i}) . Changing variables in the integral Eq. (5) yields

$$\mathcal{F}[I](u_E, v_E) = \sum_i \iint_S I(\xi_E, \eta_E) e^{-i2\pi(u_E x_E + v_E y_E)} \mu_i d\xi_E d\eta_E, \quad (15)$$

since surface brightness is preserved in the transformation, and

$$\mu_i \equiv \left| \frac{\partial(\xi_E, \eta_E)}{\partial(x_E, y_E)} \right|^{-1}, \quad (16)$$

is the absolute value (*i.e.* $\mu_i > 0$) of the inverse of the Jacobian of the transformation evaluated at image coordinates (x_{E_i}, y_{E_i}) . μ_i is also the magnification factor of image i . In the integral Eq. (15), x_E and y_E are considered as functions of (ξ_E, η_E) . If we define $\Phi \equiv \mathcal{F}[I]/F_S$ (rather than I_S as was done in Section 2.1), the visibility formula Eq. (11) still holds with

$$\Phi_{\mu l} = \sum_i \mu_i e^{-i2\pi(u_E x_{E_i} + v_E y_{E_i})}, \quad (17)$$

from Eqs. (14) and (15) for the lensed images, and

$$\Phi_B = \sum_k g_k e^{-i2\pi(u_E x_{E_k} + v_E y_{E_k})}. \quad (18)$$

for the blend stars from Eq. (9) with $I_S \pi\rho^2 = F_S$.

Let us now consider the particular case of a single lens, with the convention that the center of the source lies onto the y_E -axis, at a positive distance $u_1 > 0$ from the center of the frame, where the lens is located (Figure 1). We have

$$\Phi_{\mu l} = \mu^{(+)} e^{-i2\pi v_E r^{(+)}} + \mu^{(-)} e^{-i2\pi v_E r^{(-)}}, \quad (19)$$

where $r^{(\pm)}$ are also located onto the y_E -axis and are given by Eq. (3). The explicit calculation of Eq. (16) yields the major (+) and minor (−) images magnifications,

$$\mu^{(\pm)} = \frac{1}{2} \left| 1 \pm \frac{u_1^2 + 2}{u_1 \sqrt{u_1^2 + 4}} \right|. \quad (20)$$

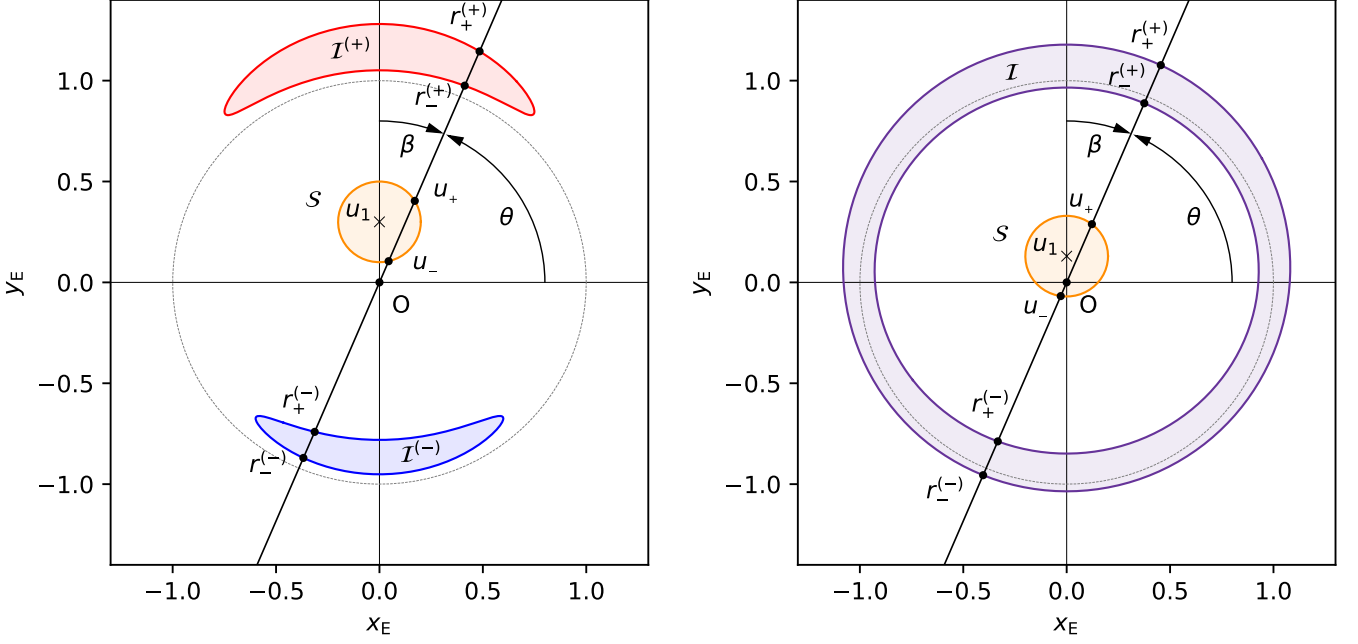


Fig. 2. Geometry and parameters for the calculation of interferometric visibility of an extended source star lensed by a single lens. In both panels, the Einstein ring is marked by the black dotted circle, and both axes are in θ_E units. $u_1 \geq 0$ is the position of the center of the source along the y_E -axis, u_+ and u_- are the intersections of the black line (polar angle θ) with the contour of the source, and $(r_+^{(+)}, r_-^{(+)})$ and $(r_+^{(-)}, r_-^{(-)})$ are their respective images given by the single-lens equation. Arc-like images are shown on the left panel ($0 < \eta_1 < 1$, where $\eta_1 = \rho/u_1$), while the case of a single ring-like image ($\eta_1 > 1$) is shown on the right.

If we neglect all possible sources of blend ($\Phi_B = 0$), the squared visibility takes a simple form,

$$|V_E|^2 = \left| \frac{\mu^{(+)} e^{-i2\pi\nu_E r_+^{(+)}} + \mu^{(-)} e^{-i2\pi\nu_E r_-^{(-)}}}{\mu^{(+)} + \mu^{(-)}} \right|^2 = \frac{1 + R^2 + 2R \cos\left(2\pi\nu_E \sqrt{u_1^2 + 4}\right)}{(1 + R^2)^2}, \quad (21)$$

where $R = \mu^{(+)}/\mu^{(-)}$ (Delplancke et al. 2001). $|V_E|^2$ is a sinusoidal function along the (Oy_E) direction, and is invariant along the (Ox_E) direction. The modulation has a period of $T = 1/(u_1^2 + 4)^{1/2}$ and the squared visibility oscillates between $\left(\frac{R-1}{R+1}\right)^2$ and 1. If u_1 is not too large ($u_1 \lesssim 0.5$, to fix ideas), the periodicity is approximately constant and equal to $T \approx 0.5$. The amplitude is maximum when u_1 is small, as $\mu^{(+)}$ and $\mu^{(-)}$ are both approximated by $1/2u_1$ so that $R \approx 1$. However, we shall see in Section 3 that the point-source model provides in this case a poor approximation of the visibility, as the lens strongly distorts the images.

2.3. Exact formula for an extended source star

The visibility and closure phase for an extended-source single-lens model was first studied by Rattenbury & Mao (2006). As the images are elongated along the Einstein ring (Figure 1) with contours well-defined analytically (Section 2.1), the authors proposed to compute numerically the visibility defined in Eq. (5) by a line integral along the outer boundary of each of the major and minor images.

Here however, we follow a different route and set up another approach to compute Eq. (5), motivated by different arguments. Firstly, our tests have shown that while the line integration scheme works fine when the images are reasonably elon-

gated (*i.e.* at low to medium magnifications), when the images takes the form of thin arcs the parametrisation of the contour reveals itself far from being optimal, as the individual points defining the images contours become strongly unevenly spaced. To achieve a reasonable accuracy, one needs to resample the points on the contours, and in any case the number of contour points must be significantly increased. This operation is mandatory, as the line integral basically operates a subtraction between the wedge-shaped area subtended by the outer boundary and that subtended by the inner boundary, which are both of order of $\varphi/2$ (as they are located at $r \approx 1$) with φ is the opening angle defined in Figure 3. In contrast, when $\rho \ll 1$ the area enclosed in a given image is of order of $\rho\varphi$, and the fractional difference corresponding to the searched visibility is of order of $\rho\varphi/(\varphi/2) = 2\rho \ll 1$. Hence an accurate visibility requires to achieve a very high accuracy on the line integrals, in particular in portions where the contours are not well sampled by the parametrisation. The approach we derive below is both robust and computationally much more efficient, and allows a precise control on the final accuracy. This can be achieved by calculating Eq. (5) as a two-dimensional integral in polar coordinates, as we detail below.

Let again $u_1 > 0$ be the ordinate of the center of the source S along the y_E -axis, and ρ the source radius (both in θ_E units), as shown in Figure 2. We again assume that the source is uniformly bright (and also the images, since surface brightness is preserved). Let θ be the angle of the usual polar coordinates, and u_+ and u_- the radii where the radial black line in Figure 2 intersects the upper and lower contours of the source. From geometrical considerations, these are given by

$$u_{\pm} = u_1 \cos \beta \pm \sqrt{\rho^2 - u_1^2 \sin^2 \beta}, \quad (22)$$

where $\beta \equiv \theta - \pi/2$. If $\rho < u_1$, we restrict β to vary between $-\arcsin \eta_1$ and $\arcsin \eta_1$ (left panel of Figure 2), where

$$\eta_1 \equiv \rho/u_1. \quad (23)$$

Otherwise, if $0 < u_1 < \rho$, we limit β to vary between $-\pi/2$ and $\pi/2$ (right panel). These choices are sufficient to parametrize the two arc-shaped images (or the ring), as we obtain two points above the horizontal axis for the major image $\mathcal{I}^{(+)}$, $r_+^{(+)}$ and $r_-^{(+)}$, and two points below for the minor image $\mathcal{I}^{(-)}$, $r_+^{(-)}$ and $r_-^{(-)}$, given by

$$\begin{cases} r_{\pm}^{(+)} = \frac{1}{2} \left(u_{\pm} + \sqrt{u_{\pm}^2 + 4} \right) \\ r_{\pm}^{(-)} = \frac{1}{2} \left(u_{\pm} - \sqrt{u_{\pm}^2 + 4} \right), \end{cases} \quad (24)$$

from Eq. (3). In all cases, $r_-^{(-)} < r_+^{(-)} < 0 < r_-^{(+)} < r_+^{(+)}$. If $u_1 = 0$, the ring is perfectly symmetric (Einstein ring) as $u_{\pm} = \pm \rho$, so that $r_-^{(-)} = -r_+^{(+)}$ and $r_-^{(+)} = -r_+^{(-)}$. To calculate the visibility, we further perform the integration of Eq. (8) in polar coordinates,

$$\begin{aligned} \Phi_{\mu l} &= \iint_{\mathcal{I}} e^{-i2\pi r(u_E \cos \theta + v_E \sin \theta)} r dr d\theta \\ &= \iint_{\mathcal{I}} e^{-i2\pi \Omega r} r dr d\theta, \end{aligned} \quad (25)$$

where

$$\Omega \equiv u_E \cos \theta + v_E \sin \theta. \quad (26)$$

We also decompose the full integral into two separates integrals, one for the image above the horizontal axis (elongated image or half-ring), $\Phi^{(+)}$, and one for the image below, $\Phi^{(-)}$, with

$$\Phi_{\mu l} = \Phi^{(+)} + \Phi^{(-)}. \quad (27)$$

Let us first consider the case $\rho < u_1$ (or $0 < \eta_1 < 1$). Since $0 < r_-^{(+)} < r_+^{(+)}$ and $\pi/2 - \arcsin \eta_1 \leq \theta \leq \pi/2 + \arcsin \eta_1$, we can write the integral Eq. (25) for the major image as

$$\begin{aligned} \Phi^{(+)} &= \int_{\pi/2 - \arcsin \eta_1}^{\pi/2 + \arcsin \eta_1} \left(\int_{r_-^{(+)}}^{r_+^{(+)}} r e^{-i2\pi \Omega r} dr \right) d\theta \\ &= \int_{-\arcsin \eta_1}^{\arcsin \eta_1} R(r_-^{(+)}, r_+^{(+)}) d\beta, \end{aligned} \quad (28)$$

where we have changed to variable β in the second line,

$$\Omega = -u_E \sin \beta + v_E \cos \beta, \quad (29)$$

and

$$\begin{aligned} R(r_1, r_2) &\equiv \int_{r_1}^{r_2} r e^{-i2\pi \Omega r} dr \\ &= \begin{cases} \frac{1}{2} (r_2^2 - r_1^2) & \text{if } \Omega = 0, \\ \left[\frac{e^{-i2\pi \Omega r} (1 + i2\pi \Omega r)}{4\pi^2 \Omega^2} \right]_{r_1}^{r_2} & \text{otherwise.} \end{cases} \end{aligned} \quad (30)$$

The first terms of the series expansion (with respect to Ω) of the expression inside the brackets are

$$\frac{e^{-i2\pi \Omega r} (1 + i2\pi \Omega r)}{4\pi^2 \Omega^2} \approx \frac{r^2}{2} + \frac{1}{4\pi^2 \Omega^2} - i\frac{2}{3} \pi r^3 \Omega - \frac{1}{2} \pi^2 r^4 \Omega^2. \quad (31)$$

When $\Omega \ll 1$, the term $1/4\pi^2 \Omega^2$ becomes large, possibly generating numerical issues although theoretically, this term cancels out in the difference Eq. (30). Hence the formula $(r_2^2 - r_1^2)/2$ may be used for values of Ω below a threshold of typically $\Omega \sim 10^{-3}$ if we want the second term of the series (in Δr^3) to contribute no more than $\sim 10^{-3}$ times the term in Δr^2 .

We proceed in a similar way for the minor image, but this time with $r_-^{(-)} < r_+^{(-)} < 0$ and $-\pi/2 - \arcsin \eta_1 \leq \theta \leq -\pi/2 + \arcsin \eta_1$, so that the integral reads

$$\begin{aligned} \Phi^{(-)} &= \int_{-\pi/2 - \arcsin \eta_1}^{-\pi/2 + \arcsin \eta_1} \left(\int_{-r_+^{(-)}}^{-r_-^{(-)}} r e^{-i2\pi \Omega r} dr \right) d\theta \\ &= \int_{-\arcsin \eta_1}^{\arcsin \eta_1} \left(\int_{-r_+^{(-)}}^{-r_-^{(-)}} r e^{i2\pi \Omega' r} dr \right) d\beta', \end{aligned} \quad (32)$$

after changing variable to $\beta' = \theta + \pi/2$, and introducing $\Omega' = -u_E \sin \beta' + v_E \cos \beta' = -[u_E \cos(\beta' - \pi/2) + v_E \sin(\beta' - \pi/2)] = -\Omega$. As β' is a dummy variable, we call it β and write

$$\begin{aligned} \Phi^{(-)} &= \int_{-\arcsin \eta_1}^{\arcsin \eta_1} \left(\int_{-r_+^{(-)}}^{-r_-^{(-)}} r e^{i2\pi \Omega r} dr \right) d\beta \\ &= \int_{-\arcsin \eta_1}^{\arcsin \eta_1} \left(\int_{r_+^{(-)}}^{r_-^{(-)}} r e^{-i2\pi \Omega r} dr \right) d\beta \\ &= \int_{-\arcsin \eta_1}^{\arcsin \eta_1} \left(- \int_{r_-^{(-)}}^{r_+^{(-)}} r e^{-i2\pi \Omega r} dr \right) d\beta, \end{aligned} \quad (33)$$

by changing variable r to $-r$ and inverting the boundaries of the integral, so that

$$\Phi^{(-)} = \int_{-\arcsin \eta_1}^{\arcsin \eta_1} -R(r_-^{(-)}, r_+^{(-)}) d\beta. \quad (34)$$

Let us now examine the case $0 < u_1 < \rho$ (or $\eta_1 > 1$). In this situation, the lens lies inside the source and there is a single ring-like image. The full ring can be drawn by varying θ from 0 to π , as $r_+^{(+)}$ and $r_-^{(+)}$ draw the half-ring above the horizontal axis, and $r_+^{(-)}$ and $r_-^{(-)}$ the half ring below it. Hence the calculation is exactly the same as for $\rho < u_1$, with the only difference that the integration is now performed between $-\pi/2 \leq \beta \leq \pi/2$.

In summary, for all values of $u_1 > 0$ and $\rho > 0$ (i.e. $\eta_1 > 0$) we have

$$\Phi_{\mu l} = \int_{-\beta_m}^{\beta_m} [R(r_-^{(+)}, r_+^{(+)}) - R(r_-^{(-)}, r_+^{(-)})] d\beta, \quad (35)$$

where

$$\beta_m \equiv \arcsin [\min(\eta_1, 1)]. \quad (36)$$

When $u_1 = 0$ (Einstein ring) this formula still holds with $\beta_m = \pi/2$. In that case, the visibility has no imaginary part, which is expected from the symmetry of the ring image.

2.4. The thin-arcs approximation

Let us consider a common case in practice, where the source has a radius ρ small compared to θ_E (typically, $\rho \lesssim 0.1$) and passes the lens at small impact parameter, typically $u_1 \lesssim 0.2$ (which would correspond to a point-source magnification at peak of about 5). This situation is illustrated in Figure 3 for two sources of radii \mathcal{S}_1 and \mathcal{S}_2 . From the figure, it is clear than if the major

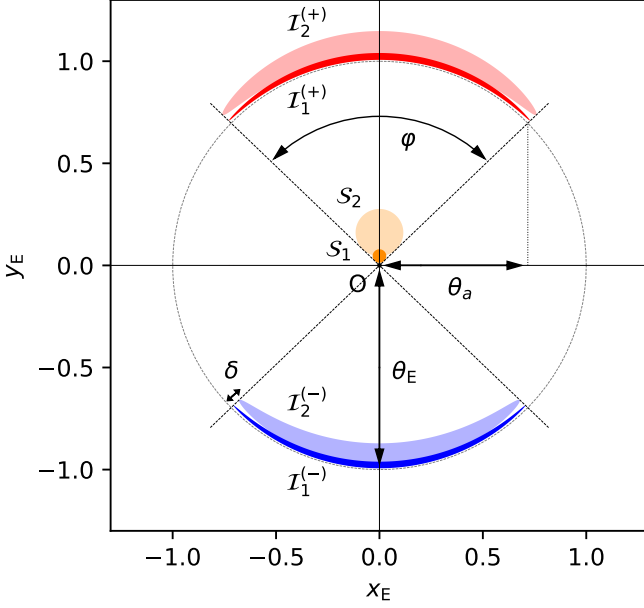


Fig. 3. Geometry of the major (red) and minor (blue) images when the images are arc-shaped (*i.e.* for $0 < \eta_1 < 1$, where $\eta_1 = \rho/u_1$). The Einstein ring is marked by the black dotted circle, and both axes are in θ_E units. When the arcs are thin, the images thickness δ is not resolved by the interferometer and two sources S_1 and S_2 (in orange) of same ratio η_1 produce arc-shaped images of equal angular elongation, $\varphi = 2 \arcsin \eta_1$. The projected extension of the arcs onto the x_E -axis is $\theta_a = \eta_1 \theta_E$, hence comparable to θ_E and thus resolved by the interferometer. When $\eta_1 > 1$, the image of the source is a ring (and $\varphi = \pi$).

and minor images are resolved by the interferometer along the (Oy_E) axis (typical angular separation of $2 \times \theta_E$, cf. Figure 3), they have a good chance to be resolved along the (Ox_E) axis as well (typical angular separation of $2 \times \theta_a$, where ‘a’ stands for ‘arcs’). In fact, since the opening angle of the images is given by $\varphi = 2 \arcsin \eta_1$ (with $\eta_1 = \rho/u_1 < 1$, and $\varphi = \pi$ for a ring-like image), we have $\theta_a = \eta_1 \theta_E$ (or $\theta_a = \theta_E$ for a ring). Values of $\eta_1 > 0.5$ are easily reached for the range of values of u_1 we discussed above. Hence we expect this situation to be common in observed microlensing events.

While the major and minor images are resolved in their individual elongations ($\sim 2\theta_a$) and mutual separation ($\sim 2\theta_E$), on the contrary their thickness (δ in Figure 3) will most certainly never be resolved by current interferometric facilities: δ being of order of ρ , this would require to reach, at best, typical angular resolutions of $\delta \approx \rho \theta_E < 10 \mu\text{as}$. Therefore, it appears natural to investigate the possibility of an approximation formula for the visibility that does not directly depend on ρ . A second argument for it is that, as shown in Figure 3, two sources of different radii but with same opening angle φ (*i.e.* same value of η_1) will be difficult to distinguish from an interferometric point of view, as the displacement is again of order of $\rho \theta_E$. Hence a natural model parameter for the sought-after approximation is η_1 , *i.e.* the ratio of ρ/u_1 instead of parameters ρ and u_1 individually. Conversely, if ρ to u_1 are used in the situation of arc-shaped images (using the exact formula Section 2.3), we shall expect these parameters to be strong correlated (if not degenerate), which may alter the smooth running of the fitting process when modelling interferometric data.

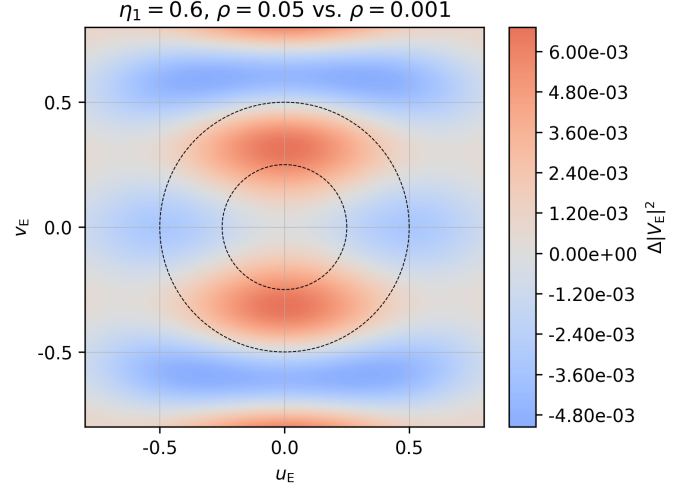


Fig. 4. Difference in squared visibility between two single-lens models with same parameter $\eta_1 = 0.6$. Both axes are in θ_E^{-1} units. The inner dashed circle marks the typical angular resolution (radius 0.25), and the outer circle (radius 0.5) twice the typical resolution. The reference model has a source radius $\rho = 10^{-3}$ (with $u_1 = 1.7 \times 10^{-3}$), while the second model has a source 50 times larger, $\rho = 5 \times 10^{-2}$ (with $u_1 = 8.3 \times 10^{-2}$). In such a case, the maximum difference in squared visibility is about 6×10^{-3} , in practice well below the noise. It justifies the use of η_1 in the modelling instead of parameters ρ and u_1 .

To further illustrate this aspect, Figure 4 shows the difference in squared visibility $\Delta|V_E|^2$ between a model computed for parameters $\rho = 0.05$ and $u_1 = 8.3 \times 10^{-2}$, and a reference model obtained with $\rho = 0.001$ and $u_1 = 1.7 \times 10^{-3}$, so that both models have same parameter $\eta_1 = 0.6$. It appears from the figure that while the source radius is multiplied by a factor of 50 between the two models, the squared visibility is not changed by more than 6×10^{-3} (for a maximal excursion between 0 and 1).

To establish a suitable approximation, that we call ‘thin-arcs approximation’, we note that when both ρ and u_1 are small (cf. Section 3.1), u_{\pm} are small as well so that we can expand $r_{\pm}^{(\pm)}$ to first order in u_{\pm} ,

$$\begin{cases} r_{\pm}^{(+)} \approx 1 + \frac{u_{\pm}}{2} \\ r_{\pm}^{(-)} \approx -1 + \frac{u_{\pm}}{2} \end{cases} \quad (37)$$

Calculating R in Eq. (30) for $\Omega \geq 0$ yields

$$\begin{cases} R(r_{-}^{(+)}, r_{+}^{(+)}) = e^{-i2\pi\Omega} \sqrt{\rho^2 - u_1^2 \sin^2 \beta} \\ R(r_{-}^{(-)}, r_{+}^{(-)}) = -e^{i2\pi\Omega} \sqrt{\rho^2 - u_1^2 \sin^2 \beta} \end{cases} \quad (38)$$

which allows to write, in Eq. (35),

$$R(r_{-}^{(+)}, r_{+}^{(+)}) - R(r_{-}^{(-)}, r_{+}^{(-)}) = 2 \cos(2\pi\Omega) \sqrt{\rho^2 - u_1^2 \sin^2 \beta}. \quad (39)$$

From Eq. (29), the real part of $\cos(2\pi\Omega)$ is the product $\cos(2\pi u_E \sin \beta) \times \cos(2\pi v_E \cos \beta)$, while its imaginary part reads $-\sin(2\pi u_E \sin \beta) \times \sin(2\pi v_E \cos \beta)$. As we integrate from $-\beta_m$ to β_m , the imaginary part cancels out while the real part is doubled. Finally, for $u_1 > 0$ the visibility reads¹

$$\Phi_{\mu l} = 4u_1 \int_0^{\beta_m} f(\beta) d\beta, \quad (40)$$

¹ The denominator of V_E in Eq. (11), $\Phi_{\mu l_0} = \Phi_{\mu l}(0, 0)$, can be written as $\Phi_{\mu l_0} = 4\rho E(\beta_m, \eta_1^{-2})$, where $E(\phi, m) = \int_0^\phi (1 - m \sin^2 \theta)^{1/2} d\theta$ is the

where again $\beta_m = \arcsin[\min(\eta_1, 1)]$ and

$$f(\beta) = \cos(2\pi u_E \sin \beta) \cos(2\pi v_E \cos \beta) \sqrt{\eta_1^2 - \sin^2 \beta}, \quad (41)$$

while for $u_1 = 0$ (Einstein ring),

$$\Phi_{\mu l} = 4\rho \int_0^{\frac{\pi}{2}} \cos(2\pi u_E \sin \beta) \cos(2\pi v_E \cos \beta) d\beta. \quad (42)$$

As expected, the integrand Eq. (41) does not depend on ρ and u_1 individually, but on their ratio η_1 (for the perfect Einstein ring, the integrand Eq. (42) does not depend of any of those parameters). In both cases (assuming no blend stars, or $\Phi_B = 0$), the factors $4u_1$ or 4ρ cancel out in Eq. (11), so that the visibility V_E depends on η_1 only for $u_1 > 0$. It is noteworthy that in the thin-arcs approximation, $\phi = \arg \Phi_{\mu l}$ can take only two values, 0 and π . It means that the bispectrum $B_{E,1,2,3}$ in Eq. (12) is also real, and the closure phases $\phi_{E,T3}$ in Eq. (13) are 0 or π . As u_1 increases, the exact value of $\phi_{E,T3}$ starts to differ from these two values, and should be calculated with the exact formula derived in Section 2.3.

Our numerical simulations show that the thin-arcs approximation speeds up the computation by a factor $\times 6$ to $\times 10$ (depending on the specific configuration of the images) compared to the exact formula, under a common implementation in Python using the `scipy/romberg` integration scheme and a given achieved accuracy (5×10^{-5}) on both the real and imaginary parts of V_E . As we further discuss in Section 3.1, the domain of validity of the thin-arcs approximation is wide. In fact considering $|V_E|^2$, for usual values of ρ and typical excursions in the $u_E v_E$ -plane, the point-source approximation may be connected to the thin-arcs approximation without having to use the exact formula at all.

2.5. Stellar limb-darkening

The most convenient way to treat limb-darkening effects is to decompose the source (assumed to be a disk) into N concentric annuli of inner and outer radii $\rho_{k-1} < \rho_k$ ($1 \leq k \leq N$) of constant surface brightness I_k , with $\rho_0 = 0$ and $\rho_N = \rho$. The visibility is then simply calculated as

$$\Phi_{\mu l} = \sum_{k=1}^N I_k (\Phi_{\mu l, k} - \Phi_{\mu l, k-1}), \quad (43)$$

where $\Phi_{\mu l, k}$ is computed for a source of radius ρ_k (or equivalently for the thin-arcs approximation, $\eta_{1, k}$, with $\eta_{1, 0} = 0$ and $\eta_{1, N} = \eta_1$). As limb-darkening affects the border of the disk of the source star, it will affect the ends of the arc-shaped images and will contribute as a correction only to the visibility.

In any case, a linear limb-darkening law will always provide a suitable description of the source's limb-darkening. Adopting the (microlensing) convention that the limb-darkening law is normalized to total unit flux yields $I_k = 1 - \Gamma \left(1 - \frac{3}{2} \left(1 - r_k^2\right)^{1/2}\right)$, where Γ is the linear limb-darkening coefficient ($0 \leq \Gamma \leq 1$), and where $r_k = \rho_k / \rho = \eta_{1, k} / \eta_1$. Γ is related to the more usual coefficient a by $a = 3\Gamma / (2 + \Gamma)$. The choice of the particular set of values ρ_k (or $\eta_{1, k}$) can be optimized to minimize N , e.g. with a linear sampling of I_k between its maximum and minimum values from center to limb, respectively $(1 + \Gamma/2)$ and $(1 - \Gamma)$.

incomplete elliptic integral of the second kind. The total source flux magnification A being the ratio between the total area of the images $\Phi_{\mu l_0}$ and the area of the source, $\pi \rho^2$, we obtain $A = (4/\pi \rho) E(\beta_m, \eta_1^{-2})$, which is the approximation derived by Yoo et al. (2004), though with a slightly different definition of E and $z = 1/\eta_1$.

3. Application

3.1. Examples and discussion

Typical examples of visibilities ($|V_E|^2$ and $\phi = \arg V_E$) are shown in Figs. 6 to 11. All figures have been calculated for the same value of $\rho = 0.03$, slightly above the typical values to challenge the approximations derived in the previous sections. From Figure 6 to Figure 10, the distance of the source to the lens is decreased from $u_1 = 0.6$ to 0.032, and Figure 11 is a perfect Einstein ring ($u_1 = 0$). For each figure, the upper panels show, on the left, the positions and shapes of the source and the images with the lens in the center, and on the right, a 3-dimensional view of the squared visibility in the Einstein $u_E v_E$ -plane. The middle panels show the squared visibility $|V_E|^2$ (left plot) and the phase ϕ (right plot). The bottom panels show the difference in squared visibility between either the point-source (left) or the thin arcs (right) approximations and the exact calculation. For reference, the color scale for these plots is set to saturate at $\Delta|V_E|^2 \pm 0.1$ (negative values in blue, positive in red), as they are typical minimum instrumental values of error bars on $|V_E|^2$.

For relatively large source-lens separations, such as $u_1 = 0.6$ in Figure 6, the images are just slightly elongated, and the point-source provides a good approximation to the visibility. The minimum squared visibility differs from 0 and the phase spans a range of values, because the two images have different magnifications. The thin-arcs approximation does not obviously provide a good approximation in that case. When $u_1 = 0.3$ (Figure 7), the point-source approximation still holds for typical (u_E, v_E) values probed by the interferometer (data points expected at best between the two dashed circles), and the thin-arcs approximation starts to provide a fair approximation within the inner dashed circle.

When, $u_1 \lesssim 0.2$ (peak point-source magnification of about 5), the situation is reversed, as seen in Figure 8 for $u_1 = 0.1$. The thin-arcs approximation now provides a very good approximation to the squared visibility (error $\leq 10^{-2}$) even outside the outer dashed circle. The point-source approximation is no longer a suitable model. In Figure 9 ($u_1 = 0.05$) and Figure 10 ($u_1 = 0.032$), the squared visibility progressively takes a circular shape, while the phase does not differ more than a few degrees from 0 or 180 deg. Finally, in Figure 11, the image is a perfect ring ($u_1 = 0$) and the thin-arcs approximation is as accurate as the exact calculation. The phase takes only the two values 0 and 180 deg.

In the situation described here ($\rho = 0.03$), the transition from the point-source to the thin-arcs approximation appears smooth for $|V_E|^2$, and unless we would have to model interferometric data with very small error bars, it appears unnecessary to perform the exact calculation. The closure phase, however, would still require to use the exact calculation, but its value is not expected to deviate more than a few degrees from 0. Finally for smaller values of ρ , the thin-arcs approximation would give even better results for $|V_E|^2$, which justifies its use for a wide range of single-lens parameters.

3.2. Practical modelling

In this section, we study possible strategies for fitting interferometric data to single-lens models, and we discuss suitable choices of model parameters for single-epoch or times-series data. In the following, we assume that the limb-darkening coefficient Γ of the source can be estimated independently (e.g. from

a colour-magnitude diagram). The main parameters we discuss below are shown in Figure 5.

Let us first consider individual interferometric epochs (which can be made of several exposures, as long as the images do not rotate significantly between two observing sequences). To compute the visibility, the point-source approximation requires u_1 as parameter, the exact formula (u_1, ρ) and the thin-arcs approximation η_1 . To fit the interferometric data, in all cases we must add α_1 as parameter (orientation in the sky of the images) as well as θ_E (to convert Einstein units into radians). If the lens is luminous, an extra parameter must be added (Section 2.1): g_L when using the point-source approximation or the exact formula; and $g'_L = g_L \pi \rho^2 / u_1$ when using the thin-arcs approximation. In general, we expect g_L to be at least partly constrained by the light curve, so this parameter may not necessarily be fitted.

In the case of time-series interferometric observations, unless we independently obtain a precise information on the exact trajectory of source relative to the lens, we can assume that the source-lens trajectory is well approximated by a straight line. This approximation holds as long as the different epochs of observation span a relatively short interval of time, typically less than two weeks. θ_E is again a parameter of the model, as it gives the overall angular scale of the problem. When using the exact formula, the source radius ρ must be added as parameter. Adding the lens as a blend star adds an additional parameter, g_L or g'_L , as described in the previous paragraph. To describe the source-lens straight trajectory, we need to add parameters α , the trajectory angle, and t_0 , a time origin (usually chosen to be the date at which the source is closest to the lens).

When using the exact formula or the point-source approximation, we also have to add in the list of parameters the Einstein timescale t_E , *i.e.* the time it takes for the source to travel θ_E , as well as u_0 , the minimum impact parameter of the source-lens trajectory. However, when using the thin-arcs approximation, u_0 is no more a convenient parameter: in fact, if for every individual epoch $\eta_1 = \rho / u_1$ only can be measured, then (from Thalles' theorem) only $\eta_0 \equiv \rho / u_0$ can be used as a parameter of the model. Similarly, t_E cannot be determined individually, as a trajectory with a higher value of u_0 will imply a slower moving source, *i.e.* a higher value of t_E for (almost) the same shape and location of the images; more precisely, the time Δt it takes for the source to travel between two epochs of observation is $\Delta t \propto u_0 t_E$, which means the product $p = u_0 t_E$ is constant. Hence in principle, p could be used as a model parameter, but in practice, it appears more convenient to use the source radius crossing time, $t_* \equiv \rho t_E$, as it is the product of the two constant quantities $\eta_0 \times u_0 t_E$, and a classical parameter in microlensing modelling.

4. Conclusion

In this work, we first reviewed the main concepts and general formulae of interferometric microlensing, and detailed the equations useful to treat the case of a single lens. We recalled the well-known visibility formula for a point-source, that we generalised to multiple lenses. We then treated the case of an extended source, and proposed a new approach for the calculation of the visibility, allowing a robust and numerically efficient calculation.

This formalism allowed us to establish a new approximation, that we coined ‘thin-arcs approximation’, which applies to microlensing events of medium or higher magnification observed around the peak, *i.e.* a large fraction of potential observational targets. We demonstrated that the computation time using this approximation is $\times 6$ to $\times 10$ times faster than with the exact formula, and applies over a wide range of lens-source separations.

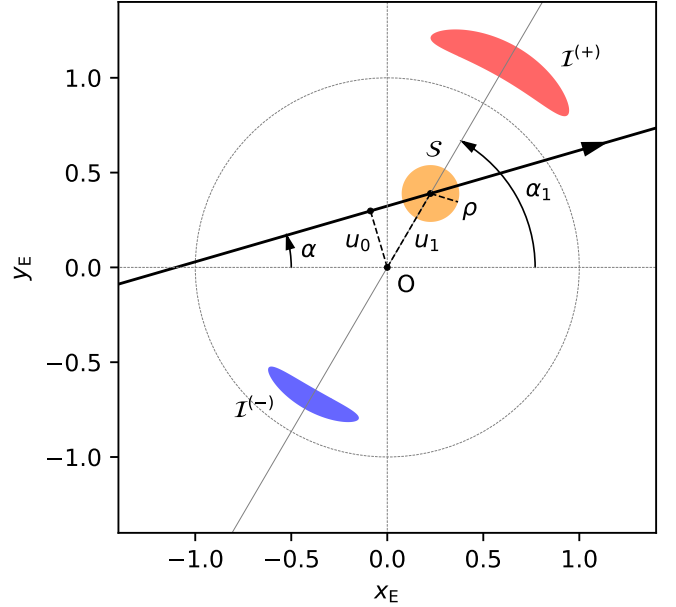


Fig. 5. Model parameters for a straight-line source-lens trajectory. The lens is the black dot in the center, the source (unseen) is the orange disk S of radius ρ , and the red and blue arcs I^+ and I^- are the major and minor lensed images, respectively. The line joining the center of the two images makes an angle α_1 with the x_E -axis, with the convention that the source center lies at a distance $u_1 > 0$ from the lens, so that the major image is up for $\alpha_1 \in [0, \pi]$. The trajectory of the source with respect to the lens is shown as the black thick arrow. It makes an angle α with the x_E -axis, and u_0 is its signed impact parameter. As the source moves relative to the lens along the black arrow, the images rotate around the lens.

It even turns out that a direct transition from the point-source to the thin-arcs approximations is possible in many situations, without having to calculate the visibility with the exact formula.

Having accurate models and reliable numerical methods is of particular importance, as the number of targets is expected to increase significantly in the near future, especially with an interferometric instrument like GRAVITY+ for the VLTI, in development at ESO.

Acknowledgements. A.C. acknowledges financial support from Sorbonne Université grant Émergence@Sorbonne-Universités 2016.

References

- Cassan, A. & Ranc, C. 2016, MNRAS, 458, 2074
- Cassan, A., Ranc, C., Absil, O., et al. 2021, Nat. Astron., in press
- Dalal, N. & Lane, B. F. 2003, ApJ, 589, 199
- Delplancke, F., Górski, K. M., & Richichi, A. 2001, A&A, 375, 701
- Dong, S., Mérand, A., Delplancke-Ströbele, F., et al. 2019, ApJ, 871, 70
- Einstein, A. 1936, Sci, 84, 506
- Gould, A. 2000, ApJ, 535, 928
- Paczynski, B. 1986, ApJ, 304, 1
- Rattenbury, N. J. & Mao, S. 2006, MNRAS, 365, 792
- Yoo, J., DePoy, D. L., Gal-Yam, A., et al. 2004, ApJ, 603, 139

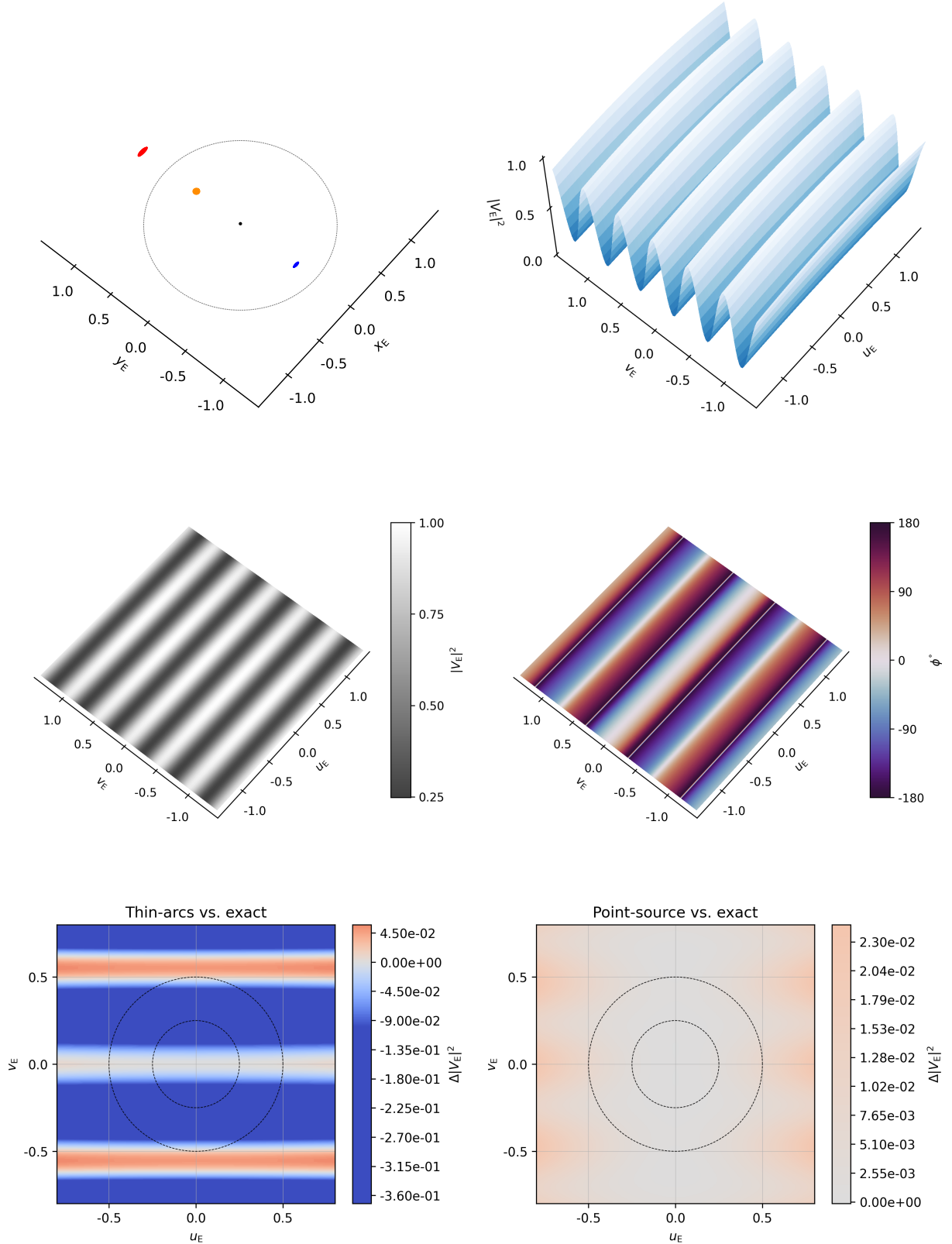


Fig. 6. Plots for $\rho = 0.03$ and $u_1 = 0.6$. **Upper panels:** the plot on the left shows the lens (black dot in the centre), the (unseen) extended source (orange disk) and its two lensed images (red and blue arc-shaped images), displayed in (x_E, y_E) coordinates which are normalized by the angular Einstein ring radius θ_E . The plot on the right displays a 3-dimensional view of the squared visibility $|V_E|^2$ in the Einstein $u_E v_E$ -plane, normalized by θ_E^{-1} . **Middle panels:** the plot on the left is a contour plot of $|V_E|^2$, while the plot on the right shows the phase of the complex visibility $\phi = \arg V_E$ (the thin white line is a visualization artefact when ϕ jumps from $-\pi$ to π , or vice versa). **Lower panels:** the two plots show the difference in squared visibility $\Delta|V_E|^2$ between either the point-source (left) or the thin-arcs (right) approximations and the exact calculation. The colours saturate for a difference of ± 0.1 . The inner dashed circle marks the typical angular resolution (radius 0.25), and the outer circle (radius 0.5) twice the typical resolution.

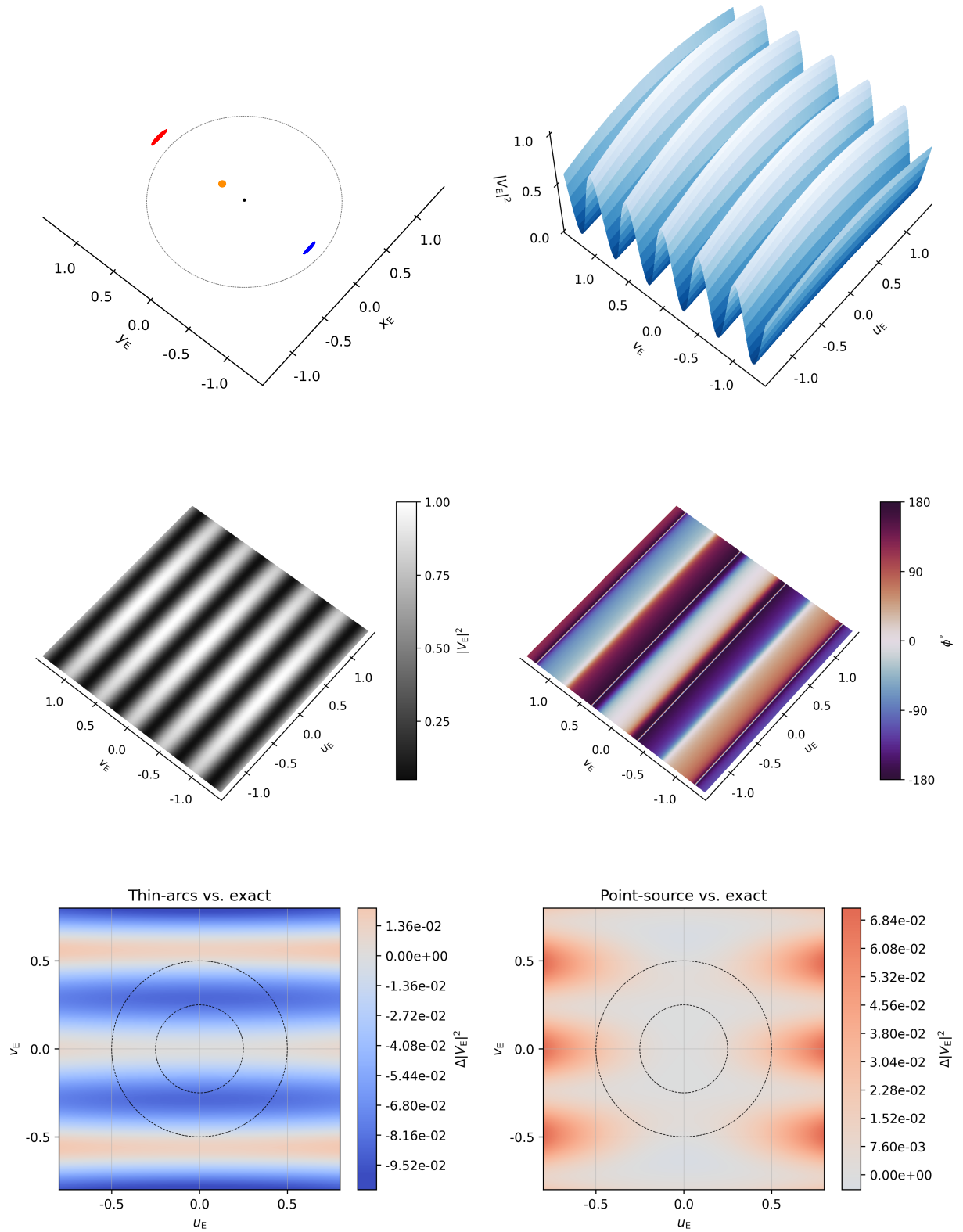


Fig. 7. Same as Figure 6 but for $u_1 = 0.3$.

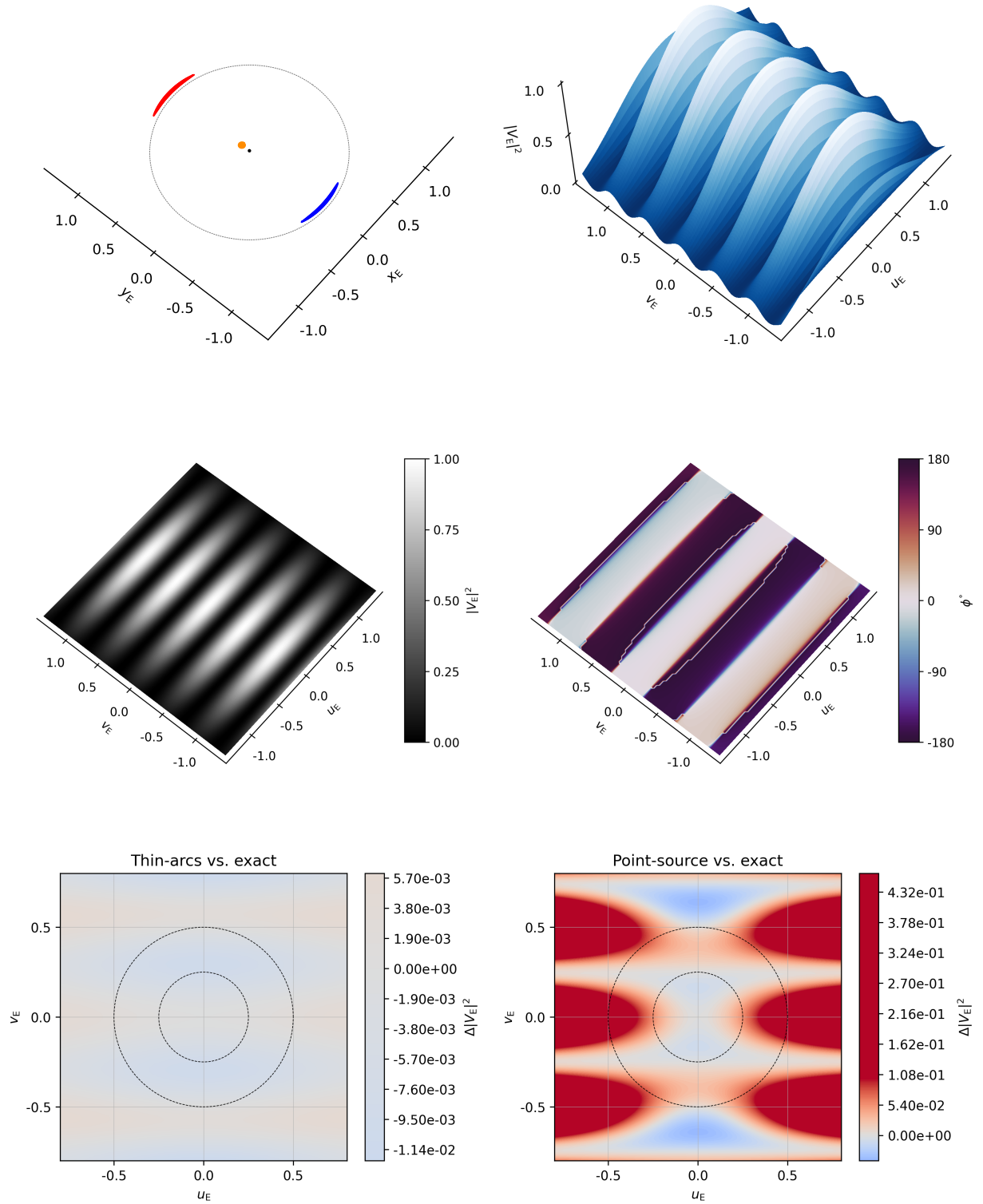


Fig. 8. Same as Figure 6 but for $u_1 = 0.1$.

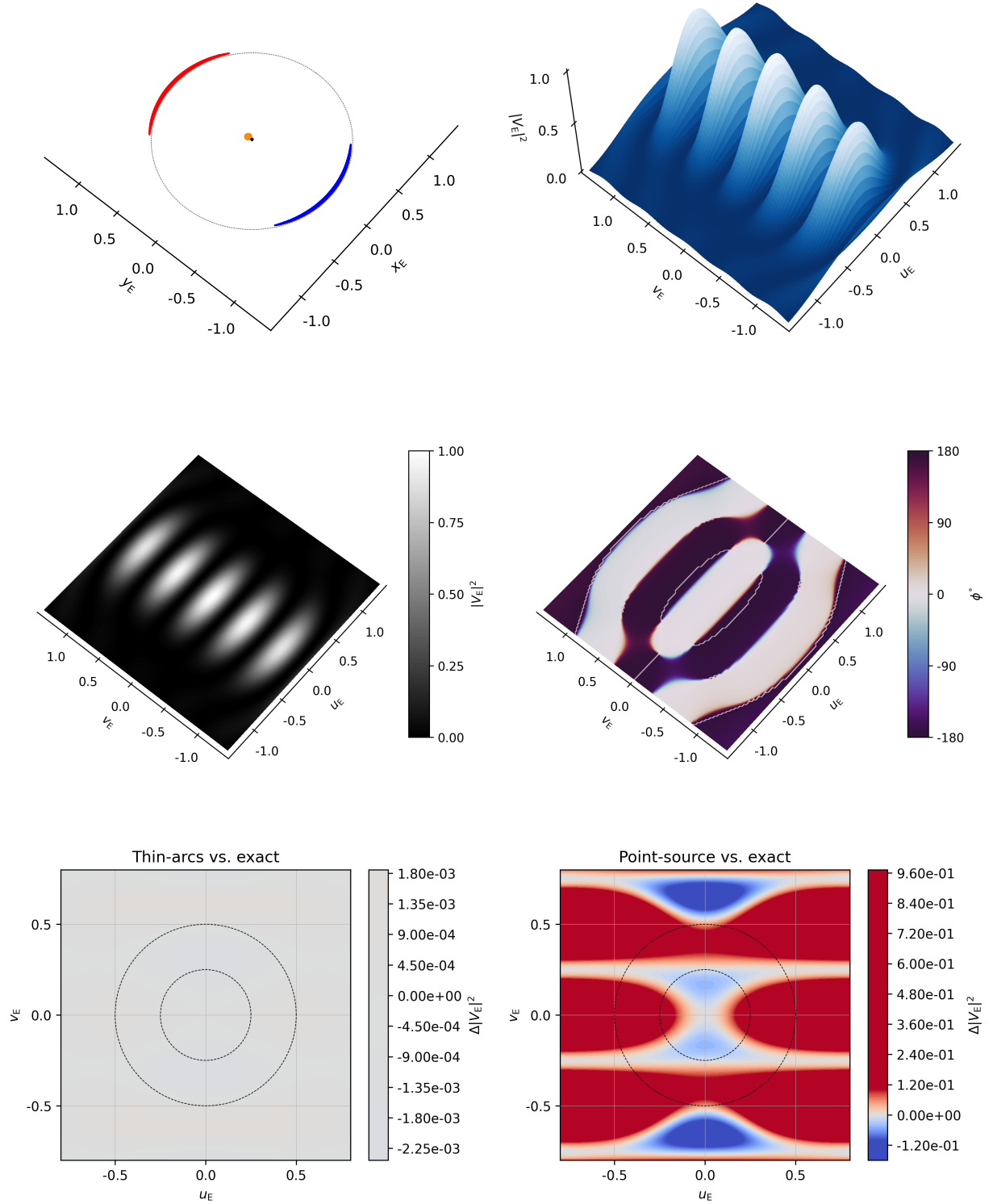


Fig. 9. Same as Figure 6 but for $u_1 = 0.05$.

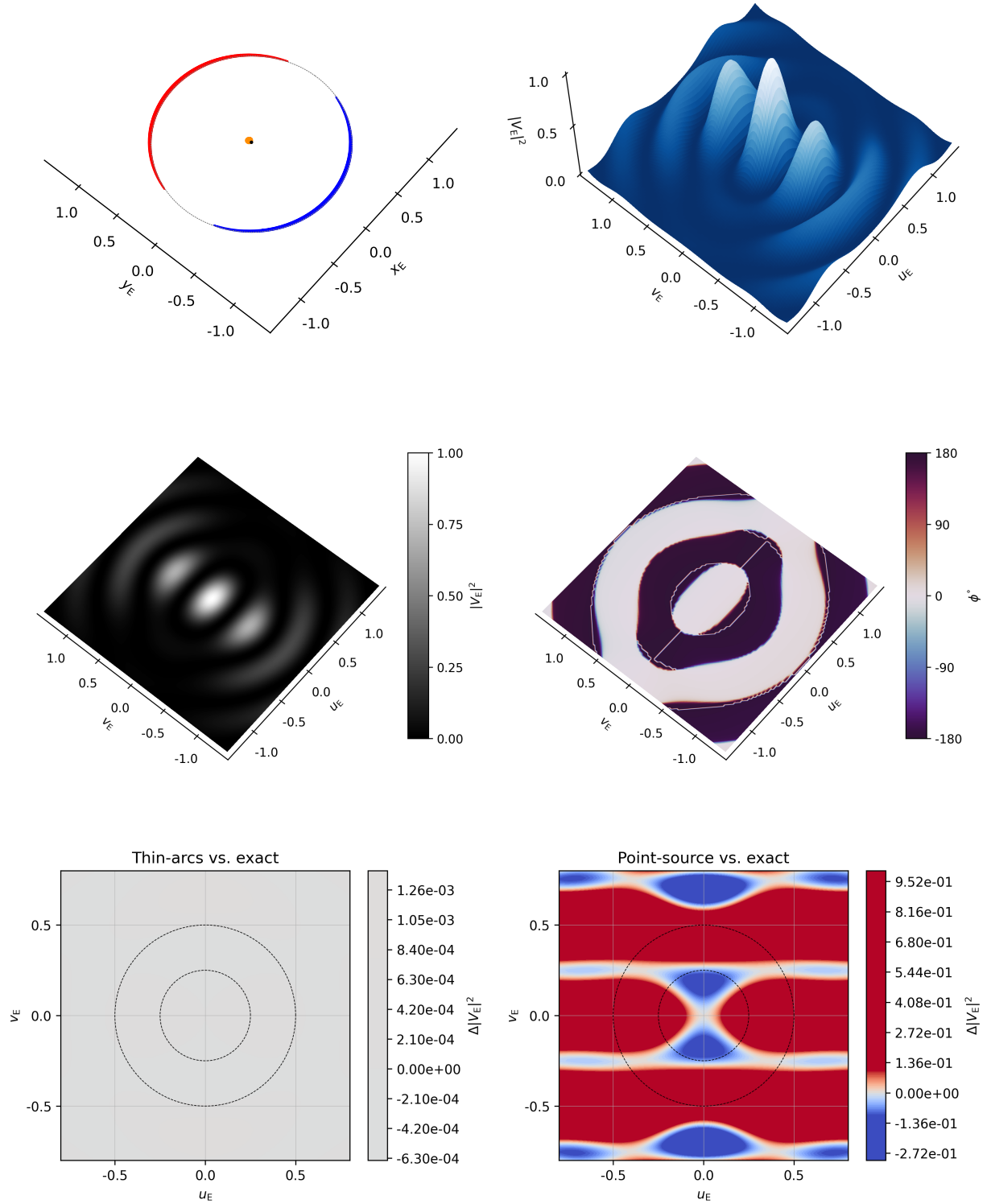


Fig. 10. Same as Figure 6 but for $u_1 = 0.032$.

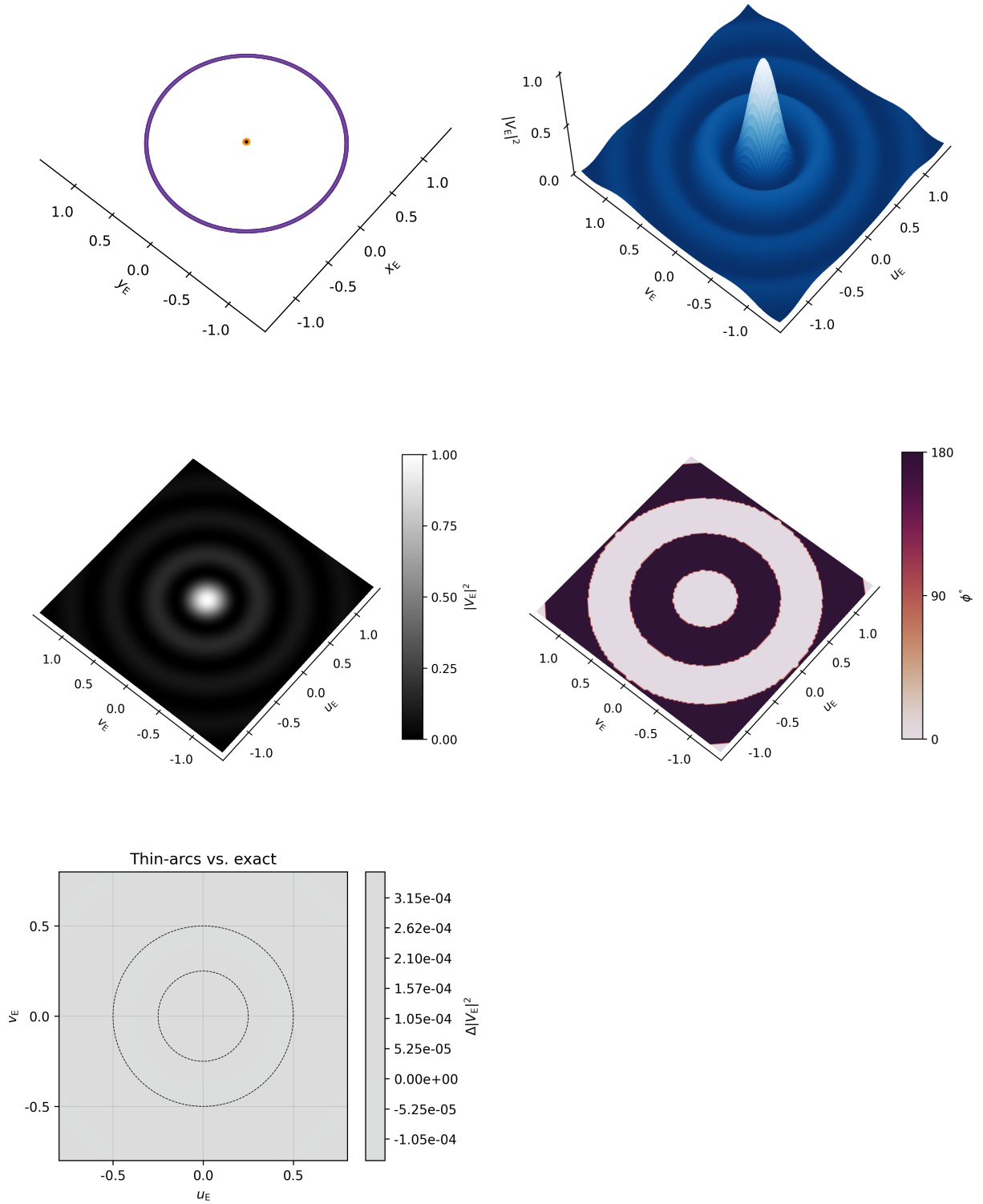


Fig. 11. Same as Figure 6 but for $u_1 = 0$. In this case, the point-source approximation yields a circle instead of two point-like images and is not shown here.